




Article

Safety Evaluation of Silicon Carbide and Zircaloy-4 Cladding during a Large-Break Loss-of-Coolant Accident [†]

Kwangwon Ahn * , Kyohun Joo  and Sung-Pil Park * 

Graduate School of Future Strategy, Korea Advanced Institute of Science and Technology, 291 Daehak-ro, Yuseong-gu, Daejeon 34141, Korea; jookh@kaist.ac.kr

* Correspondence: k.ahn@kaist.ac.kr (K.A.); sppark@kaist.ac.kr (S.-P.P.)

[†] This paper was formally circulated under the title of “Comparison of Silicon Carbide and Zircaloy4 Cladding during LBLOCA.” The initial document was prepared as a project report for the Structural Mechanics course of Prof. Kazimi at MIT. However, we updated the formal document to be standard and academic, and we would like to share our results with others.

Received: 24 October 2018; Accepted: 25 November 2018; Published: 28 November 2018



Abstract: In this study, we aim to conduct structural analyses of cladding materials, such as silicon carbide and zircaloy-4, during a Large-Break Loss-of-Coolant Accident. The safety margin is the key consideration regarding the performance of the cladding materials. Our study shows that, in terms of primary stresses, SiC has a greater safety margin than zircaloy-4 due to SiC having a higher yield and ultimate strength; the cladding outer pressure is not affected by the cladding materials and, thus, the primary stresses of all cladding materials are the same. However, for secondary stresses, zircaloy-4 has the smallest fluctuation and irradiated SiC recorded the largest; secondary stresses and temperature histories are material-dependent. Ultimately, both cladding materials were found to have sufficient safety margins with respect to primary and secondary stresses.

Keywords: silicon carbide; Zircaloy-4; Large-Break Loss-of-Coolant Accident; cladding; Pressurized Water Reactor

1. Introduction

Silicon carbide (SiC) is considered a viable material for the wall of a fusion reactor [1,2], where high temperatures and a high-radiation environment are expected [3]. The utility of SiC as a coating material for fuel in a high-temperature gas-cooled reactor is also recognized. Thus, the resistance of SiC to harsh environments could justify the application of SiC as a cladding material in a light-water nuclear reactor. However, the brittle nature of SiC is an important issue to investigate, because the degradation of SiC's thermal conductivity after irradiation can diminish its performance. Despite this issue, SiC has been considered an appropriate cladding material for improved technology fuel concepts in light-water nuclear reactors [4] due to its distinguished properties.

Advanced cladding material is important in nuclear-power plants, because improvements made to cladding materials can reduce system failure rates, and increase power density along with performance during a Large-Break Loss-of-Coolant Accident (LBLOCA) [5]. The LBLOCA is considered the worst scenario of nuclear-power failure. Although the possibility of an LBLOCA is very low, safety systems should nonetheless be designed to secure proper cooling of the reactor core to prevent core meltdown and collapse during an accident [6]. Safety can be achieved by meticulous designing of the systems, and it can also be ensured through the cladding materials. Therefore, this research aims to conduct structural analyses during a LBLOCA between SiC and zircaloy-4 (Zry-4), which are the cladding materials considered for a Pressurized Water Reactor (PWR).

Various studies have long been focused on SiC, and on its properties and application. Initially, it was developed for fossil energy and aerospace applications, because SiC is resilient to high temperatures and weight, and resistant to corrosion [7]. Since SiC has been shown to have outstanding irradiation performance, which was investigated during early studies on chemically vapor-deposited SiC for fission-fuel coatings [8–10], SiC has emerged as an attractive material for nuclear service applications [11]. For as long as SiC has been shown to be stable under neutron irradiation and high temperatures [12], most of the studies on the use of SiC in the nuclear industry have focused on the structural components of high-temperature gas-cooled reactors and fusion reactors [13,14]. Moreover, studies on the application of SiC for light-water reactors have been increasing [15]. Recent studies have suggested that SiC is a promising material for advanced nuclear applications in light of its outstanding chemical and physical performance under irradiation [16,17]. Currently, applications for SiC are under development in the nuclear-power field, including high-temperature joint and gas-reactor control-rod sheaths. These components are the main factor of the system, and are exposed to high temperatures and neutron fluences [18].

This paper is organized as follows. In Section 2, we describe the fuel assembly in detail. Section 3 compares the material properties of SiC and Zry-4 alloy. The underlying theoretical basis for structural analysis is briefly introduced in Section 4.1, and the boundary conditions for the structural analysis are presented in Section 4.2. This is followed by the stress profiles of both SiC and Zry-4 claddings during an LBLOCA, and their safety margins are then discussed in Section 4.3. Lastly, Section 5 concludes the paper.

2. Fuel Design

A PWR fuel assembly comprises a bundle of cylindrical rods placed in a square lattice. Each cylindrical rod is a tube filled with uranium oxide ceramic pellets. The gap between the pellets and the cladding tube is filled with helium gas to improve the conduction of heat transfer from the fuel pellets to the cladding. There are 264 fuel rods per fuel assembly, and 193 fuel assemblies are loaded into a reactor core. The fuel rods are placed in a 17×17 square lattice in an assembly. PWR fuel assemblies are about 4 m tall. More specific design features and parameters are shown in Table 1.

Table 1. Fuel and cladding properties for a typical four-loop Pressurized Water Reactor (PWR).

Dimension	Unit	Value
Cladding thickness	mm	0.57
Cladding inside diameter	mm	4.18
Gap thickness	mm	0.121
Fuel-pellet diameter	mm	8.19
Fuel-rod diameter	mm	9.5
Active fuel height	m	3.66
U-235 enrichment	wt %	2.6
Fuel-rod pitch	mm	12.6
Channel effective flow area	m ²	0.02458
Number of rod locations	number	289
Number of fuel rods	number	264

Two flow channels were used to represent the whole core in the RELAP5 (Idaho national laboratory, Idaho Falls, ID, USA) simulation: one (192 fuel assemblies) represents a core-average channel; and the other (1 fuel assembly) simulates a hot channel, where a single hot rod is connected to the hot channel together with the hot assembly rods. The core bypass channel was modified in accordance with the physical geometry.

The gap is initially filled with helium gas at a pressure of 1.7 MPa in a typical PWR. Gap pressure increases due to fission-gas release. However, with regard to fission-gas release, gap pressure was assumed to be constant at 8.32 MPa during the steady state and the LBLOCA. This is a conservative

assumption since, during the LBLOCA, higher gap pressure exerts greater stress on the cladding when the core is fully depressurized.

3. Material Properties

Zry-4 and SiC were selected as the cladding materials in this study. Zry-4 is currently used as a cladding material in light-water reactors due to its small neutron capture cross-section and mechanical stability. SiC is also a good material because it maintains its integrity at high temperatures and in highly irradiated environments, such as a fusion reactor. Several material properties, shown in Table 2, have been tested in the structural analyses of Zry-4 and SiC.

Table 2. Properties of zircaloy-4 (Zry-4) and silicon carbide (SiC).

	Zry-4	SiC
Coefficient of thermal expansion	6 $\mu\text{m}/\text{m K}$	3 $\mu\text{m}/\text{m K}$
Modulus of elasticity	99.3 GPa	410 GPa
Poisson's ratio	0.37	0.21
Yield strength	170 MPa	450 MPa
Ultimate tensile strength	241 MPa	450 MPa

The Zry-4 properties are based on the work of Chang [19] and Tong and Weisman [20]. Its coefficient of thermal expansion ranges from 20 to 800 $^{\circ}\text{C}$, which covers the normal and accident conditions of a PWR. The yield strength and ultimate tensile strength values are given as 288 $^{\circ}\text{C}$, which is close to the normal operating condition of a PWR.

The thermal-expansion coefficient of SiC is adopted from Carpenter [21], and the modulus of elasticity and Poisson's ratio are for Direct Sintered Silicon Carbide at 20 $^{\circ}\text{C}$ [22]. The ultimate tensile strength of SiC is also its value at 20 $^{\circ}\text{C}$, in line with DiCarlo [23]. Although this temperature is very different from the normal operating condition of a PWR, these values do not vary significantly with temperature. Since brittle materials, such as SiC, experience little plastic deformation before fracture occurs, the yield strength of SiC was set to be equal to the ultimate tensile strength.

Figure 1a shows the thermal conductivities of SiC and Zry-4. For SiC, two cases were investigated: unirradiated SiC and irradiated SiC. This is because SiC can easily be irradiated, and its thermal conductivity changes after burning the fuel. Moreover, Figure 1b presents the specific heat of Zry-4 [20] and SiC. These two figures (FRAPCON3.3) were used as input data in the RELAP5 model in order to capture the boundary conditions.

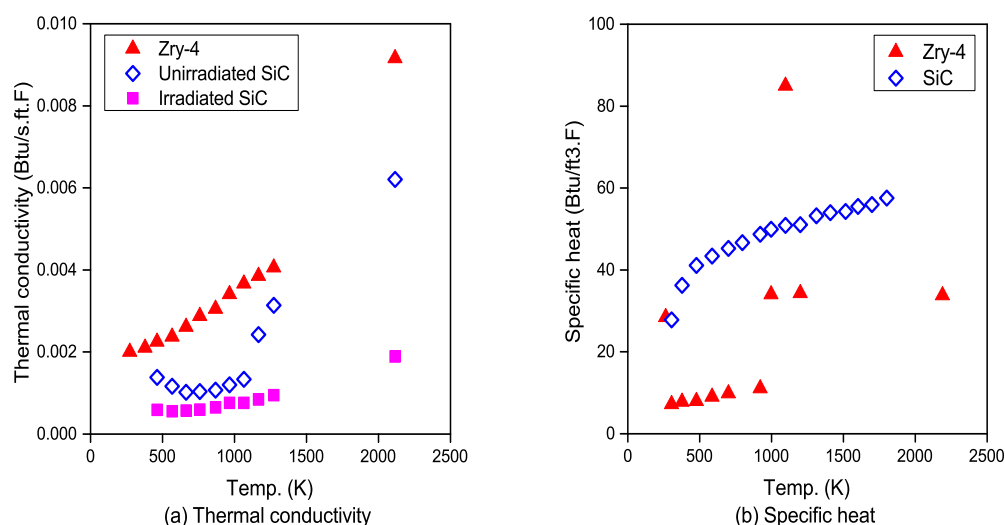


Figure 1. Input data in the RELAP5 model.

4. Fuel Rod Analysis

4.1. Methodology

Analysis was performed considering a typical 17×17 PWR fuel rod, the geometry of which is illustrated in Figure 2. The geometry includes the fuel, gap, and cladding. Its specific parameters are shown in Table 1. The purpose here was to analyze cladding from a structural mechanical point of view.

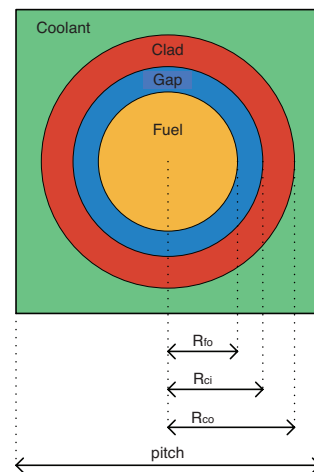


Figure 2. Schematic cross-section of a fuel cell.

It is not appropriate to apply a thin-shell model to the analysis since $t/R_{ci} > 0.1$. So, a thick-wall model was used to calculate the stress profile. The derivations are based on Kazimi [24].

Force equilibrium in the radial direction:

$$\frac{d\sigma_r}{dr} + \frac{\sigma_r - \sigma_\theta}{r} = 0 \quad (1)$$

Hook's law:

$$\varepsilon_r = \frac{1}{E} [\sigma_r - \nu(\sigma_\theta + \sigma_z)] \quad (2)$$

$$\varepsilon_\theta = \frac{1}{E} [\sigma_\theta - \nu(\sigma_r + \sigma_z)] \quad (3)$$

$$\varepsilon_z = \frac{1}{E} [\sigma_z - \nu(\sigma_\theta + \sigma_r)] \quad (4)$$

Strain–displacement relationships:

$$\varepsilon_\theta = u/r \quad (5)$$

$$\varepsilon_r = du/dr \quad (6)$$

By manipulating Equations (5) and (6), we get:

$$\frac{d\varepsilon_\theta}{dr} = \frac{1}{r}(\varepsilon_r - \varepsilon_\theta). \quad (7)$$

Since we are considering a closed cylinder far from the end, σ_z is assumed to be constant. Applying Equations (2) and (3) to Equation (5), we get:

$$\frac{d}{dr}(\sigma_r + \sigma_\theta) = 0. \quad (8)$$

Combining Equation (6) with Equation (1), we get:

$$\frac{d}{dr} \frac{1}{r} \frac{d}{dr}(r^2 \sigma_r) = 0. \quad (9)$$

Boundary conditions:

$$\sigma_r(r = R_{ci}) = -P_i \quad (10)$$

$$\sigma_r(r = R_{co}) = -P_o \quad (11)$$

Since the axial stress has less dependency on the radial direction compared to radial and hoop directional stresses, it is regarded as a constant along variable r . After solving Equations (8) and (9) with Equations (10) and (11), the solutions are:

$$\sigma_r = -P_i \left(\frac{R_{ci}}{r}\right)^2 + \left[1 - \left(\frac{R_{ci}}{r}\right)^2\right] \frac{-P_o R_{co}^2 + P_i R_{ci}^2}{R_{co}^2 - R_{ci}^2}, \quad (12)$$

$$\sigma_\theta = P_i \left(\frac{R_{ci}}{r}\right)^2 + \left[1 + \left(\frac{R_{ci}}{r}\right)^2\right] \frac{-P_o R_{co}^2 + P_i R_{ci}^2}{R_{co}^2 - R_{ci}^2}, \quad (13)$$

$$\sigma_z = \frac{\pi R_{ci}^2 P_i - \pi R_{co}^2 P_o}{\pi(R_{co}^2 - R_{ci}^2)}. \quad (14)$$

When the Fourier conduction equation is solved under a cylindrical geometry with no internal heat generation, a temperature profile usually follows a logarithmic function. For the logarithmic temperature profile, thermal stress can be obtained from Harvey [25]:

$$\sigma_r^{th} = \frac{\alpha E \Delta T}{2(1-\nu) \ln(R_{co}/R_{ci})} \left[-\ln\left(\frac{R_{co}}{r}\right) - \frac{R_{ci}^2}{R_{co}^2 - R_{ci}^2} \left(1 - \frac{R_{co}^2}{r^2}\right) \ln\left(\frac{R_{co}}{R_{ci}}\right) \right], \quad (15)$$

$$\sigma_\theta^{th} = \frac{\alpha E \Delta T}{2(1-\nu) \ln(R_{co}/R_{ci})} \left[1 - \ln\left(\frac{R_{co}}{r}\right) - \frac{R_{ci}^2}{R_{co}^2 - R_{ci}^2} \left(1 + \frac{R_{co}^2}{r^2}\right) \ln\left(\frac{R_{co}}{R_{ci}}\right) \right], \quad (16)$$

$$\sigma_z^{th} = \frac{\alpha E \Delta T}{2(1-\nu) \ln(R_{co}/R_{ci})} \left[1 - 2 \ln\left(\frac{R_{co}}{r}\right) - \frac{2R_{ci}^2}{R_{co}^2 - R_{ci}^2} \ln\left(\frac{R_{co}}{R_{ci}}\right) \right], \quad (17)$$

$$T_w(r) = T_{wo} + \Delta T \frac{\ln(R_{co}/r)}{\ln(R_{co}/R_{ci})}, \quad (18)$$

where α and ΔT are the thermal-expansion coefficient and the temperature difference between the inner wall and outer wall, respectively.

Since the primary stresses are defined as external stresses, the only primary stress for this analysis comes from the pressure difference between the inner and outer cladding, and the secondary stresses are due to a constraint. For this analysis, only thermal stress was considered as the secondary stress. For the failure criteria, the ASME code was utilized:

$$P_m \leq S_m \leq \min\left(\frac{2}{3}\sigma_y, \frac{1}{3}\sigma_u\right), \quad (19)$$

$$P_m + Q \leq 3S_m \leq 3 \min\left(\frac{2}{3}\sigma_y, \frac{1}{3}\sigma_u\right), \quad (20)$$

where S_m denotes the maximum stress intensity, and P_m and Q are the primary and thermal stresses, respectively.

Since $(\sigma_r, \sigma_\theta, \sigma_z)$ and $(\sigma'_r, \sigma'_\theta, \sigma'_z)$ are the primary and secondary principal stresses, P_m and $P_m + Q$ can be calculated using the Tresca theory:

$$P_m = \max(|\sigma_r - \sigma_\theta|, |\sigma_\theta - \sigma_z|, |\sigma_z - \sigma_r|), \quad (21)$$

$$P_m + Q = \max(|\sigma'_r - \sigma'_\theta|, |\sigma'_\theta - \sigma'_z|, |\sigma'_z - \sigma'_r|), \quad (22)$$

$$\sigma'_r = \sigma_r + \sigma_r^{th}, \quad (23)$$

$$\sigma'_\theta = \sigma_\theta + \sigma_\theta^{th}, \quad (24)$$

$$\sigma'_z = \sigma_z + \sigma_z^{th}. \quad (25)$$

4.2. Boundary Conditions

A typical four-loop Westinghouse PWR was selected as the reference plant. Three RELAP5 models were developed to establish the boundary conditions during the steady state and the LBLOCA for different cladding materials. The steady-state conditions, which are the initial conditions for the LBLOCA, were obtained through simulations and are presented in Table 3.

The gap pressure was assumed to be constant during the steady state and the LBLOCA. Although the three RELAP5 models were based on different cladding materials, all the thermal hydraulic properties given in Table 3 and Figure 3 were the same for each model since operating conditions were the same for each cladding material.

Table 3. Steady-state initialization.

Parameters	Desired	Simulated
Core power (MWth)	3479.2	3479.2
Pressurizer pressure (bar)	155.1	155.1
Cold leg temperature (K)	564.85	566.61
Hot leg temperature (K)	599.25	598.71
Total loop flow (kg/s)	18,630.0	18,714.3
Effective core flow (kg/s)	17,700.0	17,857.2
Bypass flow fraction (%)	5.00	4.58
SG secondary pressure (bar)	58.0	61.8

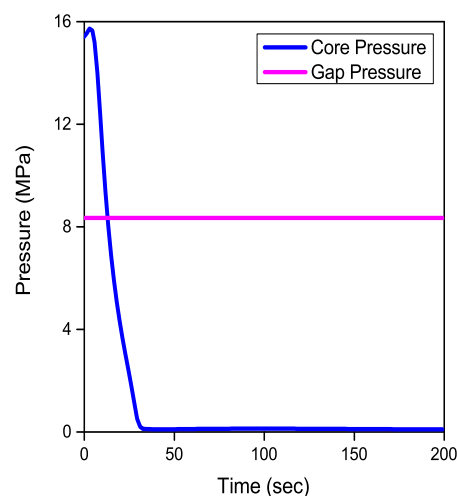


Figure 3. Pressure of fuel gap and reactor core during the LBLOCA.

Figure 4a,b exhibits the cladding outer surface temperature of the hottest fuel pin. Figure 4a shows the maximum temperature during the blowdown, and Figure 4b displays the maximum temperature during the reflood period. Although the irradiated SiC cladding during the reflood phase presents the highest cladding temperature, it still has a sufficient margin compared to the regulatory limit of 1473 K, which is more than a 16.14% safety margin.

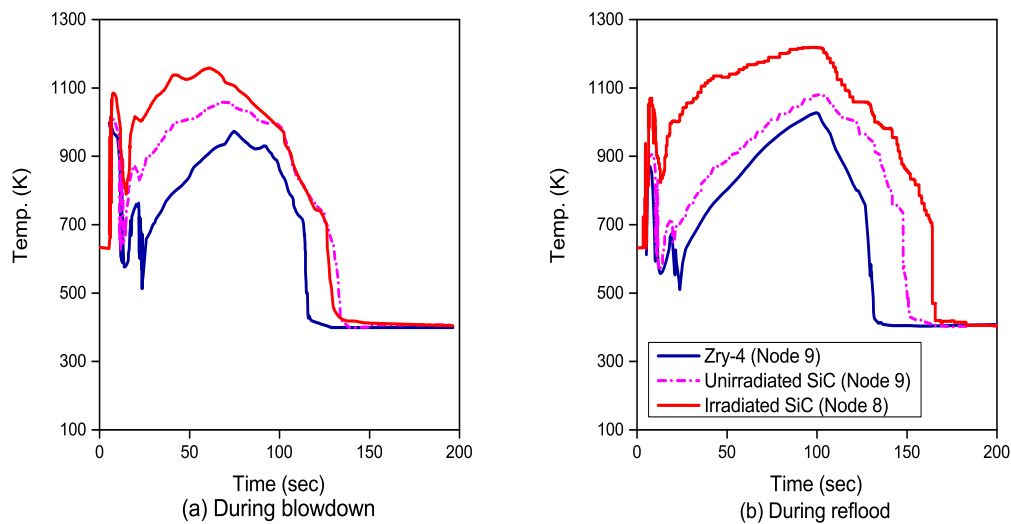


Figure 4. Outer peak cladding temperature.

Figure 5a,b exhibits the cladding inner surface temperature of the hottest fuel pin. Figure 5a presents the maximum temperature during blowdown, and Figure 5b displays the maximum temperature during the reflood period. Although the irradiated SiC cladding during the reflood phase shows the highest cladding temperature, it still has a sufficient margin compared to the regulatory limit of 1473 K, which is more than a 15.68% safety margin.

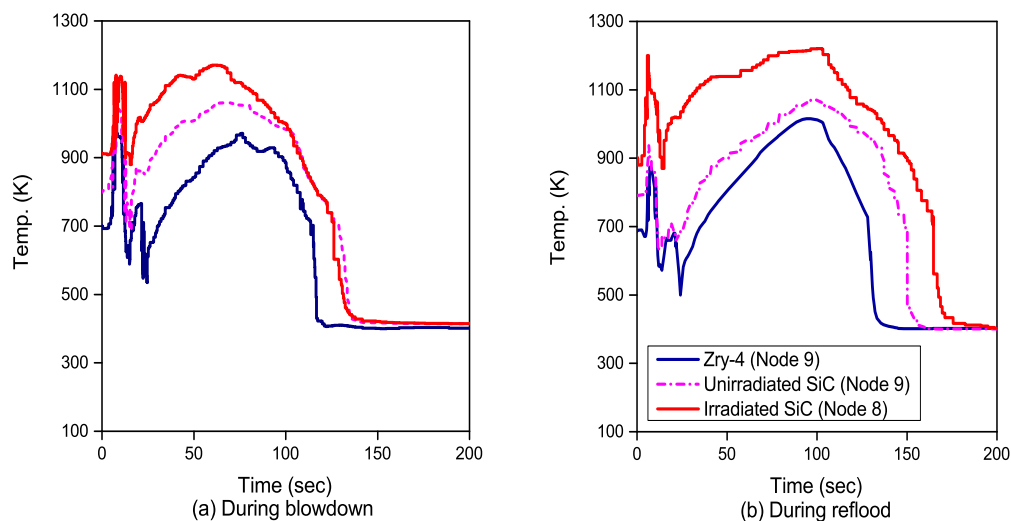


Figure 5. Inner peak cladding temperature.

4.3. Results and Discussion

Since the primary and secondary stresses are stabilized within 40 s of the LBLOCA, both stresses were analyzed for the 40 s after the LBLOCA. The next four figures, Figures 6 and 7 illustrate the primary-stress distributions. All of the primary stresses are the same for the three materials because they have the same inner and outer cladding pressure.

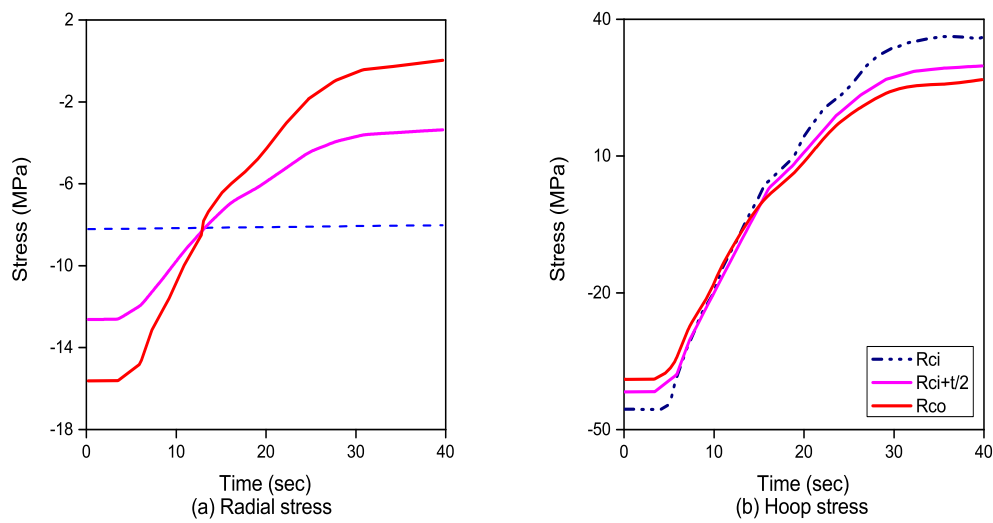


Figure 6. Pressure-induced stress distributions.

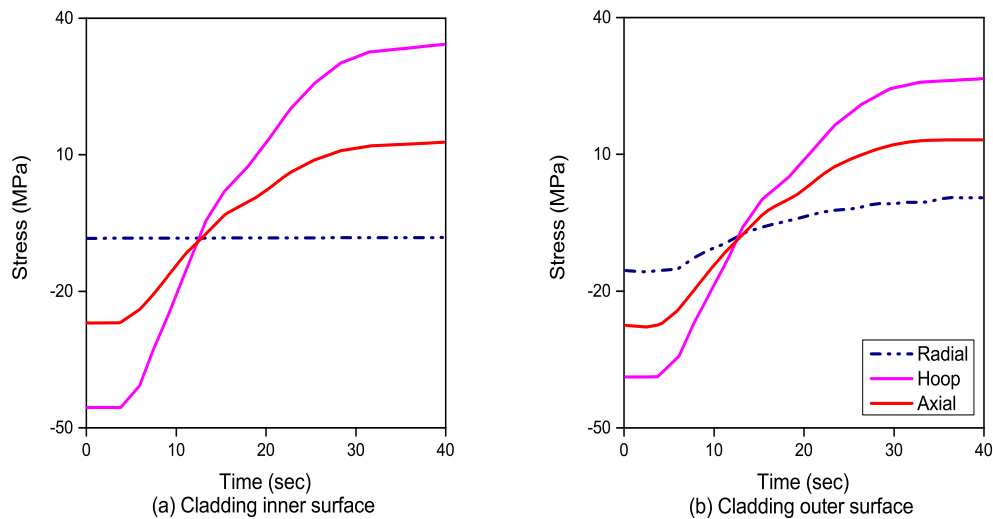


Figure 7. Pressure-induced stress distribution.

The next three figures in Figure 8 exhibit the secondary stress distributions, which include the pressure-induced-stress and thermal-stress distributions. The three investigated cladding materials (Zry-4, unirradiated SiC, and irradiated SiC) have different inner and outer temperature profiles because of their different thermal conductivities. It should be noted that the following three figures have different y-axis scales. Zry-4 has the least fluctuation in its stress history, and irradiated SiC shows the largest fluctuation in its stress history.

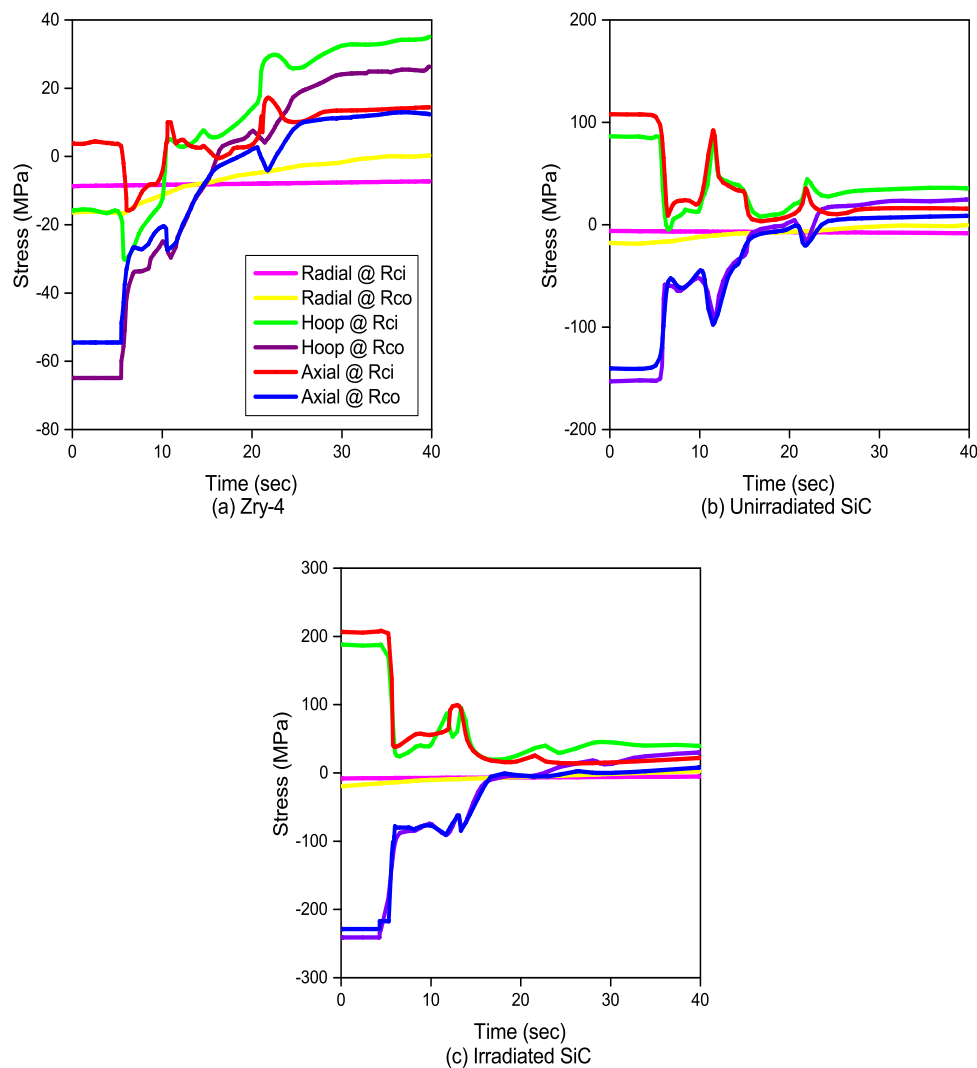


Figure 8. Secondary stress distribution.

From Figure 9a–c, it can be clearly seen that all of the Tresca stresses reach quasi-steady-state values within 40 s of the initiation of the LBLOCA. Since temperature profiles change until 180 s after the LBLOCA, this is mainly due to pressure-induced stresses. The maximum Tresca stress in all three figures, Figure 9a–c, is at approximately 4 s after the initiation of the LBLOCA. This corresponds to the initial peak temperature in the reflood boundary condition. As the ASME code was applied to the design, Figure 9d displays the primary category given by Equation (19), and Figure 9e,f depict the secondary category given by Equation (20). From Figure 9d–f, the safety margins which correspond to the previous three figures, Figure 9a–c, are shown. In Figure 9d, SiC has a higher margin than Zry-4 at every time point, although, in Figure 9e,f, the safety margin fluctuates as time passes due to the oscillating temperature profiles.

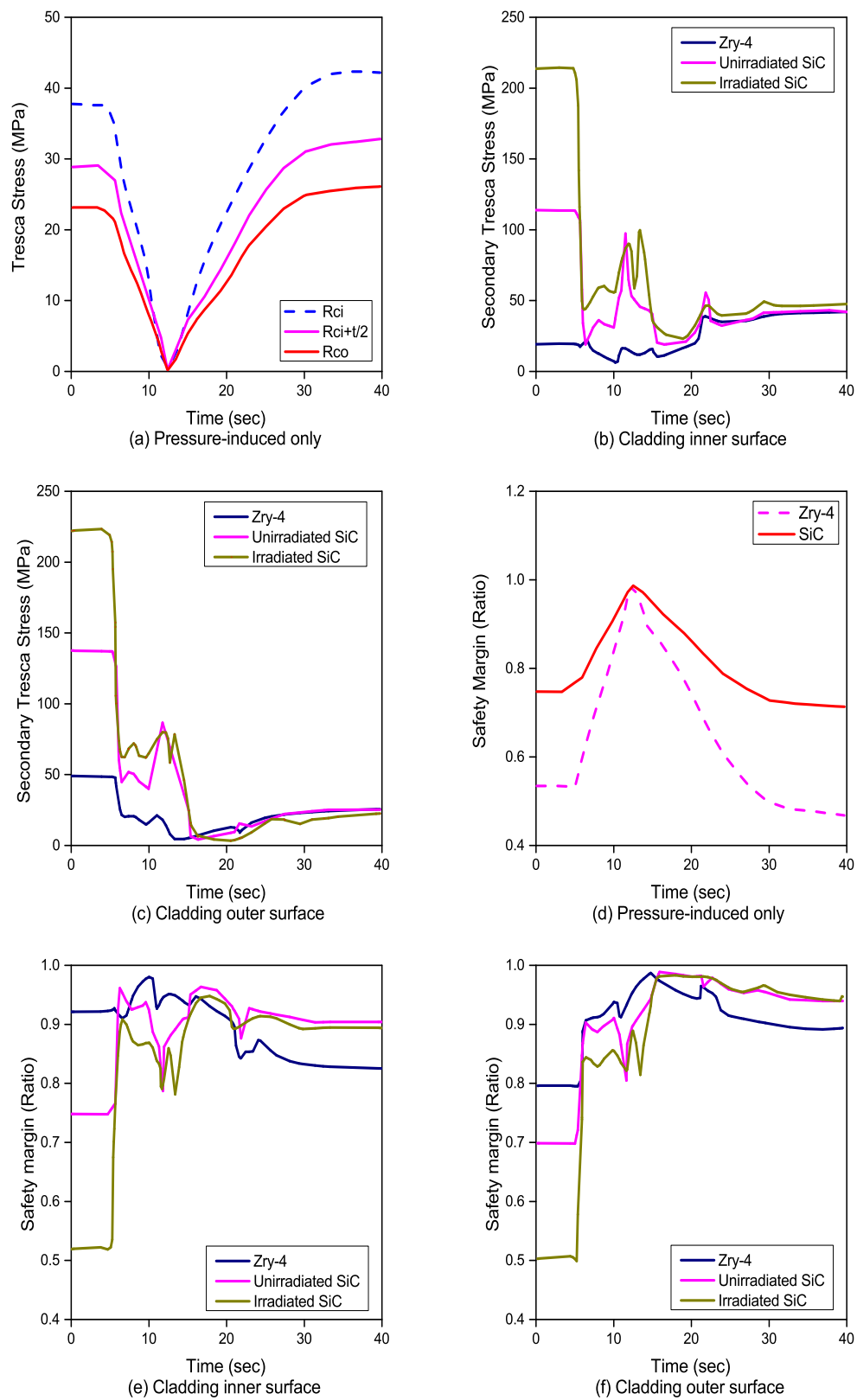


Figure 9. Tresca stress and safety margin.

The primary stresses of the three cladding materials (Zry-4, unirradiated SiC, and irradiated SiC) are all the same. This is because, during the LBLOCA process, the history of the cladding outer pressure is not affected by the cladding materials. The cladding outer surface experiences larger radial stress changes than the inner surface, while the cladding inner surface experiences larger hoop stress changes than the outer surface. Hoop stress is one of the largest stresses, and radial stress is the smallest among all three directional stresses when only primary stresses are considered.

However, since the secondary stresses and the temperature histories in the cladding differ for each of the cladding materials, secondary stresses behave differently for all three materials. In all three materials, maximum stress is at the cladding outer surface. Zry-4 has the smallest fluctuation with the smallest magnitude compared to the others, and irradiated SiC shows the largest fluctuation with the largest magnitude. Since pressure at the cladding outer surface converges to a single value within 40 s of the LBLOCA and temperature oscillates until 180 s, secondary stress is initially dominated by thermal stress and is ruled by the primary stress after 40 s.

Primary-stress intensity reaches its maximum at the cladding inner surface and its minimum at the cladding outer surface. All secondary-stress intensities are stabilized around 30 s after the LBLOCA. Secondary-stress intensity presents the same behavior as the primary Tresca stress, and the primary Tresca value at the end of the transient phase is approximately the same for all cases, since the primary stress dominates toward the end of the transient phase for each material. At the beginning of the LBLOCA, the stress applied to Zry-4 is the smallest, while that for irradiated SiC is the largest, but all three materials finally converge to a similar value.

In terms of primary stresses, SiC has a higher safety margin than Zry-4 due to its higher yield and ultimate strength at the same primary Tresca stress. However, for secondary stresses, Zry-4 performs better than the two SiC materials within 5 s of the LBLOCA due to its high thermal conductivity, which reduces the temperature gradient between the inner and outer surfaces of the cladding. After 5 s, since the primary stresses dominate over the thermal stresses, the SiC cladding has better results in terms of the safety margin. Irradiated SiC always performs worse than the unirradiated SiC, as the thermal conductivity of irradiated SiC is lower.

5. Conclusions

The purpose of this study was to conduct a safety evaluation of cladding material during a LBLOCA. The results of numerical experiments reveal that the history of the cladding outer pressure is not affected by the cladding materials during the LBLOCA and, thus, the primary stresses of all three materials are the same. On the other hand, since secondary stresses and the temperature histories are different for each material, the secondary stresses behave differently depending on the cladding material. Zry-4 has the smallest fluctuation, and irradiated SiC shows the largest. In terms of the primary stresses, SiC has a higher yield and ultimate strength under the same primary Tresca stress, so it has a greater safety margin than Zry-4.

In our study, gap pressure was assumed to be constant. However, as the burn-up increases, gap pressure rises due to fission-gas release. Young's modulus, yield strength, and ultimate strength were also considered constant, but they depend on temperature. Moreover, we did not consider the creep, strain, displacement, and junction discontinuity. By considering precise input parameters, we could set up more realistic models and obtain reasonable results. In the simulation cases, we could also investigate the power-up rate case and other transient analyses, like Loss-of-Flow Accident (LOFA), and these could broaden our understanding of SiC in nuclear applications. Furthermore, if we use a well-developed simulation code for structural analysis, like FRAPTRAN, we could conduct a study in a more realistic and straightforward manner.

Author Contributions: K.A. and S.-P.P. conceived and designed the research; K.A. and K.J. analyzed the data; K.A., K.J. and S.-P.P. wrote the paper.

Acknowledgments: The initial draft of this article was written in 2006 during Kwangwon Ahn's doctoral course at MIT under the guidance of Kazimi, who was one of the world's foremost educators and researchers in nuclear science and engineering. This research would not be completed without the guidance and encouragement of Kazimi. Unfortunately, we lost him unexpectedly in 2015, and we always pray that his soul may rest in peace.

Funding: This research received no external funding.

Conflicts of Interest: The authors declare no conflict of interest.

References

1. Snead, L.L.; Zinkle, S.J.; Steiner, D. Radiation Induced Microstructure and Mechanical Property Evolution of SiC/C/SiC Composite Materials. *J. Nucl. Mater.* **1992**, *191–194 Pt A*, 560–565. [\[CrossRef\]](#)
2. Hollenberg, G.W.; Henager, C.G.; Youngblood, G.E.; Trimble, D.J.; Simonson, S.A.; Newsome, G.A.; Lewis, E. The Effect of Irradiation on the Stability and Properties of Monolithic Silicon Carbide and SiC_f/SiC Composites up to 25 dpa. *J. Nucl. Mater.* **1995**, *219*, 70–86. [\[CrossRef\]](#)
3. Rover, L.H.; Hopkins, G.R. Ceramic Materials for Fusion. *Nucl. Technol.* **1976**, *29*, 274–302. [\[CrossRef\]](#)
4. Cozzo, C. SiC Cladding Thermal Conductivity Requirements for Normal Operation and LOCA Conditions. *Prog. Nucl. Eng.* **2018**, *106*, 278–283. [\[CrossRef\]](#)
5. Lee, S.W.; Kim, H.T.; Bang, I.C. Performance Evaluation of UO₂/Graphen Composite Fuel and SiC Cladding during LBLOCA using MARS-KS. *Nucl. Engin. Des.* **2013**, *257*, 139–145. [\[CrossRef\]](#)
6. Yang, J.H.; Wang, J.R.; Lin, H.T.; Shin, C. LBLOCA Analysis for the Maanshan PWR Nuclear Power Plant Using Trace. *Eng. Procedia* **2012**, *14*, 292–297. [\[CrossRef\]](#)
7. Bloom, E. The Challenge of Developing Structural Materials for Fusion Power Systems. *J. Nucl. Mater.* **1988**, *263 Pt A*, 7–17. [\[CrossRef\]](#)
8. Price, R.J. Effects of Fast-Neutron Irradiation on Pyrolytic Silicon Carbide. *J. Nucl. Mater.* **1969**, *33*, 17–22. [\[CrossRef\]](#)
9. Price, R.J. Properties of Silicon Carbide for Nuclear Fuel Particle Coatings. *Nucl. Technol.* **1977**, *35*, 320–336. [\[CrossRef\]](#)
10. Katoh, Y.; Snead, L.L.; Henager, C.H., Jr.; Hasegawa, A.; Kohyama, A.; Riccardi, B.; Hegeman, H. Current Status and Critical Issues for Development of SiC Composites for Fusion Applications. *J. Nucl. Mater.* **2007**, *367–370*, 659–671. [\[CrossRef\]](#)
11. Katoh, Y.; Snead, L.L.; Nozawa, T.; Kondo, S.; Busby, J.T. Thermophysical and Mechanical Properties of Near-Stoichiometric Fiber CVI SiC/SiC Composites After Neutron Irradiation at Elevated Temperatures. *J. Nucl. Mater.* **2010**, *403*, 48–61. [\[CrossRef\]](#)
12. Senor, D.J.; Trimble, D.J.; Youngblood, G.E.; Newsome, G.A.; Moore, C.E.; Moods, J.J. Effects of Neutron Irradiation on Thermal Conductivity of SiC-Based Composites and Monolithic Ceramics. *Fusion Technol.* **1996**, *30 Pt 2A*, 943–955.
13. Katoh, Y.; Ozawa, K.; Hinoki, T.; Choi, Y.; Snead, L.L.; Hasegawa, A. Mechanical Properties of Advanced SiC Fiber Composites Irradiated at Very High Temperatures. *J. Nucl. Mater.* **2011**, *417*, 416–420. [\[CrossRef\]](#)
14. Katoh, Y.; Snead, L. Operating Temperature Window for SiC Ceramics and Composites for Fusion Energy Applications. *Fusion Sci. Technol.* **2009**, *56 Pt 2*, 1045–1052. [\[CrossRef\]](#)
15. Feinroth, H. Silicon Carbide TRIPLEXTM Fuel Clad for Accident Resistance and Durability. In Proceedings of the 1st ICMST Conference, Kerala, India, 10–14 June 2012.
16. Feng, L.; Zhu, F. Fuel Assembly Design for Supercritical Water-Cooled Reactor. *J. Nucl. Eng. Radiat. Sci.* **2016**, *2*, 011014.
17. Ning, K.; Lu, K. Ion Irradiation Effect on Spark Plasma Sintered Silicon Carbide Ceramics with Nanostructured Ferritic Alloy Aid. *J. Am. Ceram. Soc.* **2018**, *54*, 605–612. [\[CrossRef\]](#)
18. Snead, L.L.; Nozawa, T.; Ferraris, M.; Katoh, Y.; Shinavski, R.; Sawan, M. Silicon Carbide Composites as Fusion Power Reactor Structural Materials. *J. Nucl. Mater.* **2011**, *417*, 330–339. [\[CrossRef\]](#)
19. Chang, W. Technical Data Sheet—Reactor Grade Zirconium Alloys for Nuclear Waste Disposal. *Allegheny Technol.* **2003**.

20. Tong, L.; Weisman, J. *Thermal Analysis of Pressurized Water Reactors*; American Nuclear Society: Cook County, IL, USA, 1996.
21. Carpenter, D.M. *Thermal Assessment of Innovative Fuel Designs for High Performance Light Water Reactors*; MIT, Center for Advanced Nuclear Energy Systems: Cambridge, MA, USA, 2006.
22. CoorsTek. *Amazing Solution: Advanced Silicon Carbide for Critical Components*; F0401 8510-1024; CoorsTek Inc.: Golden, CO, USA, 2006.
23. DiCarlo, J.A. *High-Performance SiC/SiC Ceramic Composite Systems Developed for 1315 °C (2400 °F) Engine Component*; NASA/TM-2004-212729; NASA: Washington, DC, USA, 2004.
24. Kazimi, M.S. *Lecture Notes and Problem Sets in Course 22.314*; MIT, Center for Advanced Nuclear Energy Systems: Cambridge, MA, USA, 2006.
25. Harvey, J.F. *Pressure Vessel Design: Nuclear and Chemical Application*; D Van Nostrand Company Inc.: Princeton, NJ, USA, 1963.



© 2018 by the authors. Licensee MDPI, Basel, Switzerland. This article is an open access article distributed under the terms and conditions of the Creative Commons Attribution (CC BY) license (<http://creativecommons.org/licenses/by/4.0/>).